materials

Article

Theoretical Prediction of Structures and Properties of 2,4,6-Trinitro-1,3,5-Triazine (TNTA) Green Energetic Materials from DFT and ReaxFF Molecular Modeling

Ming-Ming Zhou and Dong Xiang *

College of Chemistry and Environmental Engineering, Yangtze University, Jingzhou 434023, China; 2021720391@yangtzeu.edu.cn
* Correspondence: xiangdong@yangtzeu.edu.cn

Abstract: Nitryl cyanide, O_2NCN, as a new high-energy molecule, has not yet been successfully synthesized. It has prompted us to conduct a theoretical study of its possible space structures and properties. The RESP charges and the most stable spatial structures demonstrate that crystal morphology is affected by both the main nonbonded interactions and the molecular arrangement. The crystal structure prediction indicated that there are seven structures, namely P1, $P2_1$, $P2_12_12_1$, $P2_1/c$, $Pna2_1$, Pbca, and C2/c. The most stable space structure is likely to be $Pna2_1$ and the corresponding cell parameters are Z = 4, a = 8.69 Å, b = 9.07 Å, c = 9.65 Å, and $\alpha = \beta = \gamma = 90.0°$. To further study the intermolecular interactions of TNTA, a series of theoretical analyses were employed, including Hirshfeld surface analysis and fingerprint plots. The pyrolysis mechanism and properties show that high temperatures can promote decomposition. The systematic search approach can be a new strategy to identify structures effectively and has the potential to provide systematic theoretical guidance for the synthesis of TNTA.

Keywords: crystal morphology; cell parameters; intermolecular interaction; Hirshfeld surface; pyrolysis mechanism

check for updates

Citation: Zhou, M.-M.; Xiang, D. Theoretical Prediction of Structures and Properties of 2,4,6-Trinitro-1,3,5-Triazine (TNTA) Green Energetic Materials from DFT and ReaxFF Molecular Modeling. *Materials* **2022**, *15*, 3873. https://doi.org/10.3390/ma15113873

Academic Editors: Paolo Restuccia and James Ren

Received: 19 April 2022
Accepted: 27 May 2022
Published: 29 May 2022

1. Introduction

The ab initio theory was used to assess the energy performance and other important properties of 2,4,6-trinitro-1,3,5-triazine (TNTA) in 1907 [1]. The explosive performance of TNTA is superior to that of cyclotetramethylene tetranitramine (HMX), and it has a higher density of 2.1 $g{\cdot}cm^{-3}$ [2]. Korkin, A. A. et al. [3] conducted a theoretical study of its possible derivatives with similar performance (exothermic decomposition) but with possibly increased stability and a higher density in its condensed state. The research found that the higher the stability of the six-membered ring structure, the higher the density and energy released when it decomposes into a stable species, determining that TNTA is a potential high-energy compound. Yang K. [4] studied potential synthetic routes using the MP2/6-311G(d,p)//B3LYP/6-31G(d) levels of theory. Values of the heat of formation in the solid phase were predicted from density functional theory calculations. Densities were estimated from a regression equation obtained by molecular surface electrostatic potentials for TNTA. This work also suggested that TNTA might be formed in a solution if the trimerization reaction is carried out in a concentrated solution of nitryl cyanide. However, TNTA was not successfully synthesized. This current study rapidly predicted the structure and pyrolysis mechanism of TNTA, which can provide theoretical guidance for the experimental preparation.

The strength of intermolecular and intramolecular nonbonded interactions can be measured by restrained electrostatic potential (RESP) [5–7]. Zhang et al. [8–12] provided a detailed summary of the intermolecular interactions that play a dominant role in the packaging structures. Predicting crystal structures remains a challenging problem [13].

Some studies [14,15] have predicted the structures and properties of high-energy materials. Other studies [16–19] have studied the thermal decomposition mechanism of high-energy materials by ReaxFF reactive molecular dynamics simulations. In this study, firstly, partial RESP charges and unit cell parameters were used to predict the space group and packing of TNTA. Then, Hirshfeld surface analysis and fingerprint plots were used to study the molecular interactions of TNTA. Finally, the thermal decomposition of TNTA was researched by reactive molecular dynamics using ReaxFF-lg.

2. Computational Details

The RESP charges were generated as follows: All molecules were optimized at the B3LYP/6-311g(d,p) density functional theory (DFT) level using Gaussian 16 software [20]. Then, the RESP charges were fitted from the optimized geometry and wave function using Multiwfn software [21]. The RESP charges of the monomers were derived from the respective trimers optimized by DFT, which is similar to the reported treatment method [22].

The Hirshfeld surfaces [23] or isosurfaces of the electron density were mapped by CrystalExplorer [24], which is a freely available software. Two-dimensional mapping [25,26], a simple color plot, was used to analyze the intermolecular interactions quantitatively and qualitatively. The distances to the nearest atoms outside, de, and inside, di [26–28], were defined as the points of the intermolecular contacts.

The ReaxFF-lg force field using the LAMMPS program package performed all the molecular simulations. The original cell structure was a CIF file downloaded from CCDC, and the single-crystal cell was expanded into $3 \times 4 \times 2$ supercells as the research substrate for dynamic simulation. The molecular formula and atomic numbering of TNTA are shown in Figure 1. First, the canonical ensemble (NVT) and the Berendsen thermostat were applied to the molecular dynamics (MD) simulation with a total time of 10 ps at 300 K, which further relaxed the TNTA supercell. Then, ReaxFF-lg isothermal–isochoric MD (NVT-MD) simulations were performed for 300 ps at 1800, 2250, 2500, 3000, and 3500 K, respectively, controlled by the Berendsen thermostat based on the relax supercell. An analysis of the fragments was performed with a 0.3 bond order cutoff value for each atom pair to identify the chemical species. The information of the dynamic trajectory was recorded every 50 fs, which was used to analyze the evolution details of TNTA in the pyrolysis process.

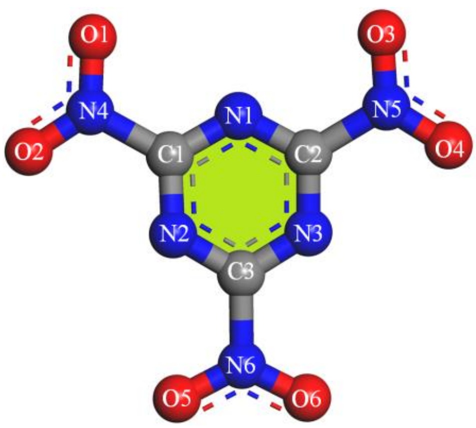

Figure 1. Structure and atomic numbering of TNTA.

Simulated annealing of the global minimum energy, a thermodynamic problem, was performed by Monte Carlo (MC). The crystal was heated quickly to a high temperature and then cooled slowly to obtain the annealing structure. The packing groups were modified by the cell parameters by rotating and translating the rigid molecular units. For each space group, the low potential energy (E) packings were selected.

3. Results and Discussions

3.1. Crystal Structure Predict

The detailed COMPASS force field parameters and partial RESP charges are given in Table 1. The partial RESP charge of C1–C3 was 0.78. Meanwhile, the partial RESP charge of N1–N3 was −0.73. The greater the difference in the electronegativity between C1–C3 and N1–N3, the stronger the stabilizing bond–antibond interactions [5,6]. This demonstrates that the benzene ring-like structure is much more stable than other bonds. Moreover, the nonbonds of (C1–C3)/(N1–N3) have a significant effect on the intermolecular stacking [7]. Both the partial RESP charges of C1–C3 and N4–N6 were positive. The difference in the partial RESP charges between C1–C3 and N1–N3 was exactly the same as the value of the NO_2 fragment. This demonstrates that the bonds of C1–C3 and N4–N6 are relatively weak. The bonding of C1–C3 and N4–N6 is mainly due to the interaction between N4–N6 and O1–O6. This nonbonded interaction has an effect not only on the intramolecular but also on the intermolecular stacking. The nonbonded interactions of (C1–C3)/(N1–N3) and (N4–N6)/(O1–O6) determine the stacking of molecules.

Table 1. Atom names, force field parameters, and RESP charges taken from COMPASS for prediction of crystal morphology.

	Force Field Types	Atom Type Description	RESP Charges
C1–C3	C_3N	sp^2, double bond to N (-C=N-)	0.78
O1–O6	O_{12}	sp^2, in nitro group (-NO_2)	−0.35
N1–N3	$N_{2=}$	sp^2, double bond to C (-N=C-)	−0.73
N4–N6	N_3O	sp^2, in nitro group (-NO_2)	0.65

The impact sensitivity (IS) could largely be affected by the crystal packing structure [5–7]. Therefore, we investigated the variations in the crystal packing structures from a viewpoint of seven space groups, as shown in Figure 2. The space groups $P2_12_12_1$, $P2_1/c$, and C2/c are not affected by the intermolecular interactions on molecular stacking. So, they are not the most reasonable spatial arrangement. The P1 and $P2_1$ space groups are affected by the nonbonded interaction of (N4–N6)/(O1–O6). However, the strongest nonbonded interaction of (C1–C3)/(N1–N3) is ignored. The packing structure of the Pbca space group is the exact opposite to that of the P1 and $P2_1$ space groups. The random molecular arrangement is not conducive to impact sensitivity. The packing structure of $Pna2_1$ combines the main nonbonded interaction, as shown in Table 1, and the graphene-like structure of TATB [29]. The $Pna2_1$ space group is the most likely spatial arrangement.

We employed the COMPASS force field and the Polymorph module in Materials Studio (MS) 4.4 2008 to obtain the possible molecular packing in the crystal state. Statistical data [30–33] demonstrate that most crystals belong to seven space groups (P1, $P2_1$, $P2_12_12_1$, $P2_1/c$, $Pna2_1$, Pbca, and C2/c), and the global search was confined to these groups only. The space group with the lowest energy was selected as the most likely molecular packing. The input structure for the polymorph search came from the ground-state geometry calculation at the B3LYP/6-311G(d,p) level. Here, we applied the PBE and PW91 pseudopotentials to the GGA and the CA-PZ pseudopotential to the LDA functional to the input structures. Table 2 shows the packing energy and cell parameters of the seven space groups. It was found that the differences among the packing energies estimated by the GGA-PBE for the seven space groups were much smaller than those estimated by the GGA-PW91 and LDA-CA-PZ. The energies were in the range of −4.24 to −0.87 $kJ \cdot mol^{-1}$ and the $Pna2_1$ space group had the lowest energy. The lower the lattice energy, the more stable the crystal structure. Therefore, due to the lowest Gibbs free energy, the $Pna2_1$ space group is the most likely crystal structure for TNTA. The corresponding lattice parameters were Z = 4, a = 8.69 Å, b = 9.07 Å, c = 9.65 Å, and $\alpha = \beta = \gamma = 90.0°$.

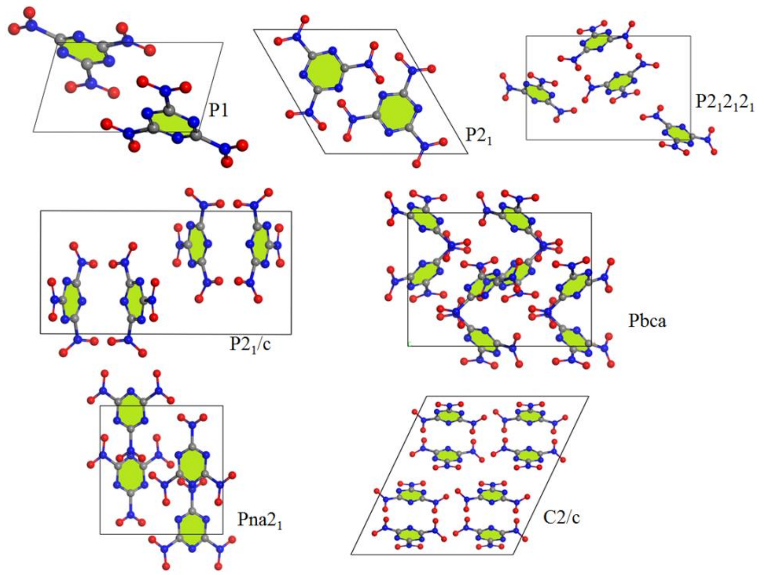

Figure 2. Most stable structures of TNTA for 7 different space groups obtained using Monte Carlo simulated annealing and Dreiding FF optimization.

Table 2. Unit cell parameters of the possible molecular packing of TNTA.

Method/ Functional	Space Groups	Z	E (kJ/mol)	ρ (g/cm^3)	a (Å)	b (Å)	c (Å)	α (°)	β (°)	γ (°)
GGA-PBE	P1	2	−3.82	1.85	10.99	5.51	9.02	86.84	116.27	124.64
	$P2_1$	2	−3.72	1.83	9.06	5.48	9.12	90.0	60.03	90.0
	$P2_12_12_1$	4	−3.87	1.83	14.12	6.26	8.90	90.0	90.0	90.0
	$P2_1/c$	4	−3.82	1.86	8.15	15.65	6.42	90.0	109.16	90.0
	$Pna2_1$	4	−4.11	1.89	8.69	9.07	9.65	90.0	90.0	90.0
	Pbca	8	−3.91	1.90	13.17	9.57	12.01	90.0	90.0	90.0
	C2/c	8	−3.88	1.84	15.70	6.48	17.04	90.0	64.49	90.0
GGA-PW91	P1	2	−4.02	1.76	10.07	6.07	8.89	90.14	117.46	118.00
	$P2_1$	2	−3.96	1.73	9.16	5.68	9.21	90.0	59.79	90.0
	$P2_12_12_1$	4	−4.05	1.75	14.29	6.33	9.09	90.0	90.0	90.0
	$P2_1/c$	4	−4.01	1.75	8.30	15.91	6.59	90.0	109.57	90.0
	$Pna2_1$	4	−4.24	1.80	8.73	9.16	9.98	90.0	90.0	90.0
	Pbca	8	−4.07	1.78	13.55	9.71	12.24	90.0	90.0	90.0
	C2/c	8	−0.87	1.76	15.80	6.58	17.40	90.0	64.70	90.0
	P1	2	22.63	2.28	9.21	5.39	8.40	90.65	120.99	113.80
LDA-CA-PZ	$P2_1$	2	23.01	2.23	8.73	4.89	8.72	90.0	59.88	90.0
	$P2_12_12_1$	4	22.32	2.30	13.36	5.61	8.33	90.0	90.0	90.0
	$P2_1/c$	4	22.49	2.28	7.71	14.02	6.16	90.0	108.96	90.0
	$Pna2_1$	4	22.17	2.31	8.30	8.58	8.70	90.0	90.0	90.0
	Pbca	8	22.32	2.32	12.13	8.96	11.37	90.0	90.0	90.0
	C2/c	8	−35.8	1.77	15.79	6.53	17.45	90.0	64.57	90.0

To obtain a better understanding of the crystal stacking, the intermolecular interactions [11,34] of single crystals were studied through Hirshfeld surface analysis using freeware [26,35]. In the Hirshfeld surface analysis, the red and blue areas represent the high and low probabilities of close contact with external molecules, respectively [36]. Two features can be seen on the surfaces in Figure 3. One is that the interaction takes place through both the external and internal atoms because the red dots are distributed on both the front and side faces. These irregular surfaces show that TNTA molecules are irregular, more uneven, and less planar. The spatial symmetry of the whole surface shape of $Pna2_1$ is relatively better than the other space groups. This shows that the crystal stacking of $Pna2_1$ is more spatially symmetrical. The other feature is that the red dots are concentrated around the oxygen atoms. O···O contacts become dominant in TNTA molecules. The more oxygen atoms exposed on the exterior of TNTA molecules, the more sensitive the molecules are. Figure 4 shows that the O···O contact percentage of the $Pna2_1$ space group is 39%, which is the lowest percentage of the seven space groups. These results demonstrate that the $Pna2_1$ space configuration is the most stable crystal stacking for TNTA molecules.

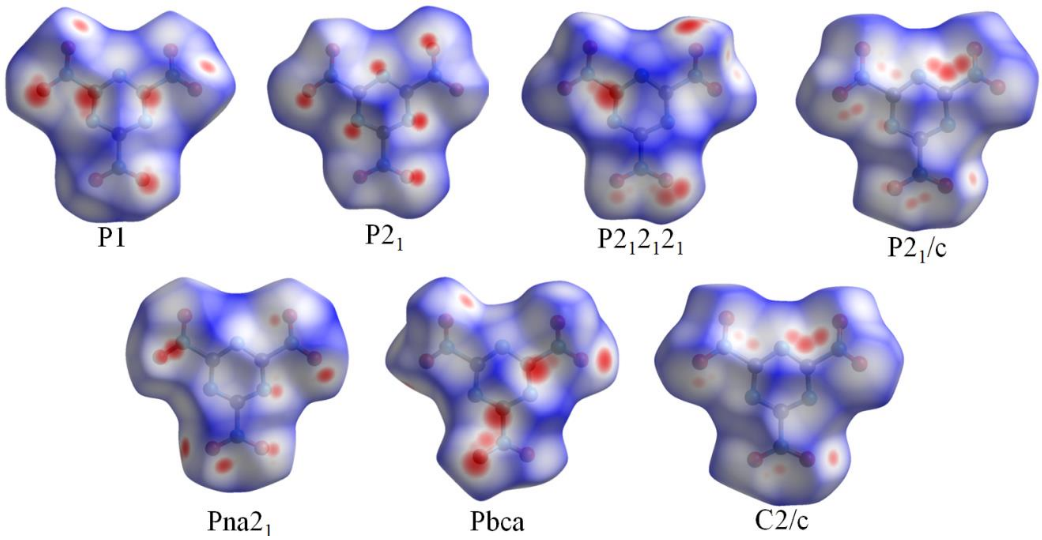

Figure 3. Hirshfeld surfaces of seven space groups in crystal stacking.

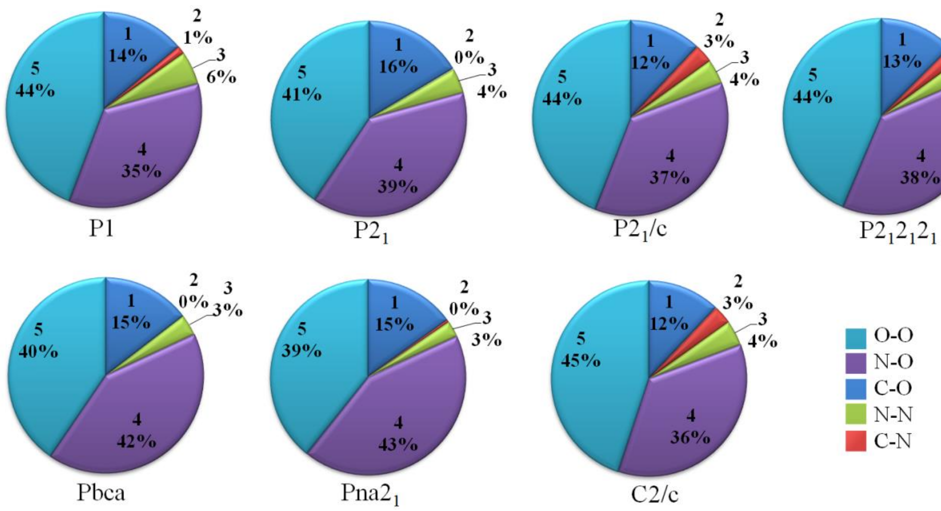

Figure 4. The individual atomic contact percentage contributions to the Hirshfeld surface of seven space groups.

The percentage of N···O contacts is the second highest among the seven space groups, at 43%, as shown in Figure 4. The C···O contacts are the other main intermolecular interactions. Looking at Figures 1 and 3, we can draw the conclusion that N···O and C···O contacts may contribute to planar conjugated molecular structures between the NO_2 group and the heterocyclic group. This may be because the crystal stacking of $Pna2_1$ is much more stable than the others.

Two-dimensional plots of these intermolecular contacts are shown in Figure 5. The narrow orange line denoting O···O contacts is much more obvious in the plot of the P1 space group, which suggests an increase in the O···O contacts. This demonstrates that the crystal stacking is much more sensitive in the P1 space group.

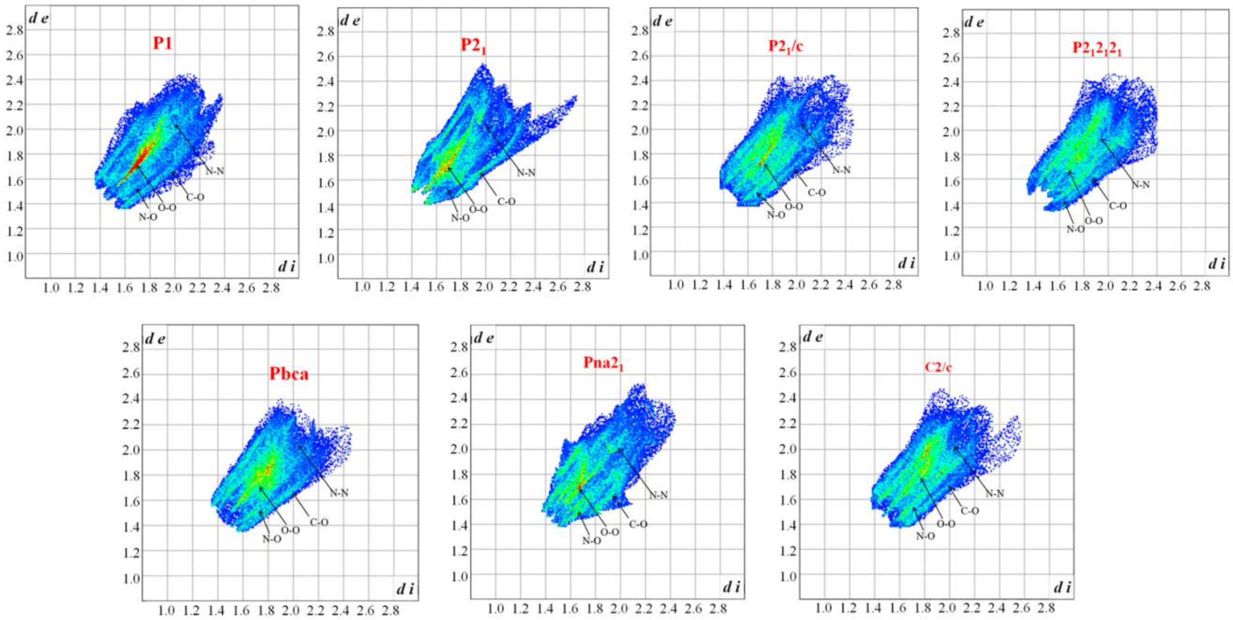

Figure 5. Two-dimensional fingerprint plots in crystal stacking.

3.2. Reactive Molecular Dynamics Using ReaxFF-lg

The RESP charges, space groups, and intermolecular interactions predicted that $Pna2_1$ has a much more stable crystal morphology. Therefore, the MD simulations were performed solely for the crystal structure of the Pna21 space group. The evolution of the potential energy (PE) of the system is shown in Figure 6. The curves, except the 1800 K curve, first decrease steadily, then reach an approximately horizontal line, indicating that TNTA breaks down rapidly and instantaneously at these extreme temperatures. The curve of 1800 K decreases steadily, implying that TNTA is not completely decomposed within 300 ps. The asymptotic value of PE increased with the temperature increase. The declining rate of PE demonstrates the accelerating release of heat as the temperature increased.

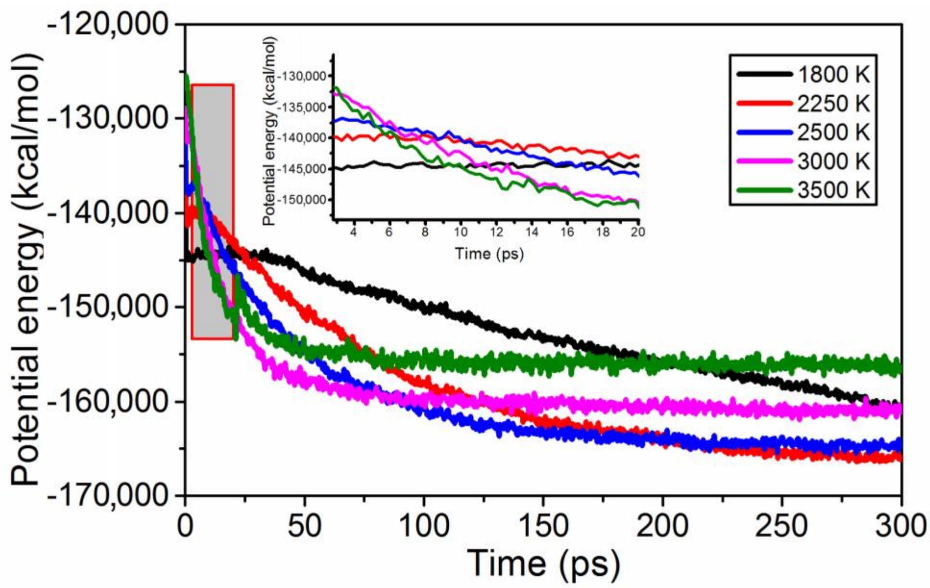

Figure 6. Evolution of the potential energy of the system over time at different temperatures.

The population of TNTA molecules reduced rapidly under five extreme conditions as shown in Figure 7. With increases in temperature, the population of the TNTA molecules disappeared faster. This implies that increasing the temperature can accelerate the decomposition rate of TNTA.

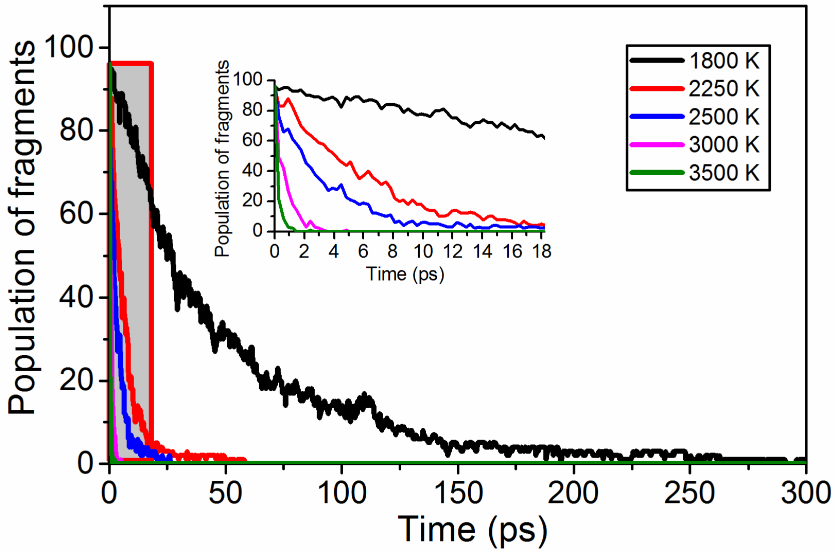

Figure 7. The population of TNTA molecules over time during the whole decomposition stage at the five extreme conditions.

Figure 8 demonstrates the time evolution of the main fragments of NO_2 during the whole decomposition stage under the five extreme conditions. All the curves, except the 1800 K curve, initially rapidly increase and then decrease until they disappear over time, indicating that TNTA first breaks the C-NO_2 bond to generate NO_2, and then all of the NO_2 fragments decompose into more stable products, such as N_2, over time. As the temperature increased, the maximum value of the NO_2 and the rates of increase and decrease in the amount of NO_2 were higher, indicating that increases in temperature can accelerate the decomposition rate of TNTA. At 1800 K, the amount of NO_2 first increased and then oscillated around the equilibrium value of 30. The results show that TNTA does not decompose completely in 300 ps. This conclusion is consistent with the results in Figures 6 and 7.

The curves of the amount of NO initially rapidly increase and then decrease until reaching an equilibrium value, indicating that TNTA first converts nitro to nitroso, and then a part of the NO fragments decompose into more stable products over time. As the temperature increased, the maximum value of NO and the rate of increase in the amount of NO were higher, indicating that increases in the temperature can accelerate the decomposition rate of TNTA. However, the equilibrium value was lower with the temperature increase, demonstrating that higher temperatures can accelerate NO fragment decomposition into more stable products.

The curves of the amount of NO_3 initially slightly increase and then decrease with time evolution. As the temperature increased, the maximum value of NO_3 and the rate of increase in the amount of NO_3 was lower, indicating that increases in the temperature can inhibit the production of NO_3. The NO_3 disappeared, except at 1800 K, it reached an equilibrium value. This demonstrates that higher temperatures can accelerate the complete decomposition of TNTA.

The decay rate of TNTA molecules increased with increasing temperature. The evolution of the amounts of the final products (N_2, and CO_2) over time is shown in Figure 9. The final products were constantly produced, and their amounts were nearly stable at the end. The N_2 and CO_2 increased sharply, then reached equilibrium, except at 1800 K. However, the value of N_2 and CO_2 increased steadily over 300 ps. This demonstrates that TNTA decomposes totally except at 1800 K. The equilibrium values were larger as the temperature increased. It took less time to reach equilibrium as the temperature increased. This implies that higher temperatures can accelerate the decomposition of TNTA. An interesting phenomenon is that the variation trend of N_2 is consistent with that of CO_2. At the same time, the amount of N_2 was slightly higher than the amount of CO_2 during the whole reaction time at all five high temperatures.

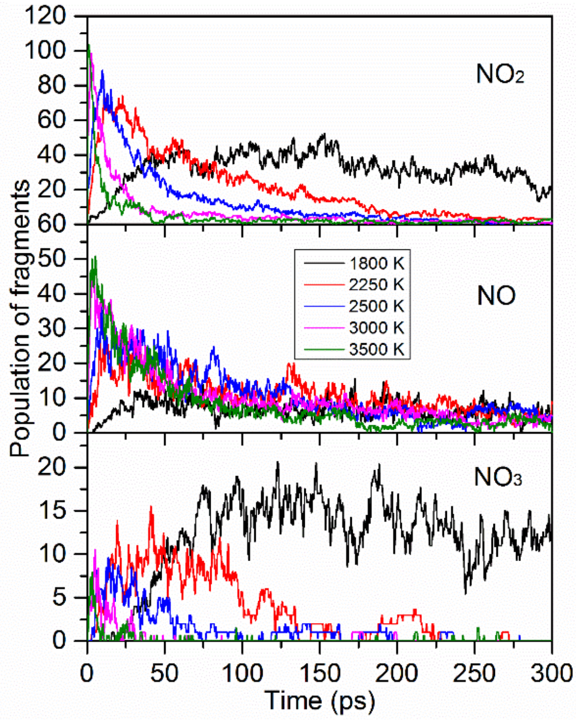

Figure 8. Time evolution of the main fragments NO_2, NO, and NO_3 during the whole decomposition stage at the five extreme conditions. The thick trendlines correspond to the actual concentration data of the matching color.

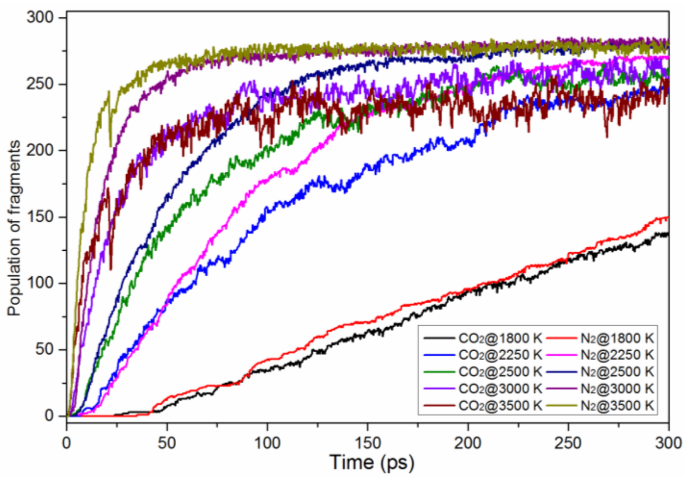

Figure 9. Time evolution of the main products, CO_2 and N_2, during the whole decomposition stage at the five extreme conditions. The thick trendlines correspond to the actual concentration data of the matching color.

For each temperature, the system was heated to the target temperature within 0.3 ps and the C-NO_2 bond was broken to release NO_2 fragments. The life time was shorter as the temperature increased and the maximum number of NO_2 fragments was larger with the temperature increase, indicating that higher temperatures would promote the production of NO_2 and then promote its decomposition into more stable products. The appearance time of the fragments NO, NO_3, CO_2, and N_2 became shorter as the temperature increased. This demonstrates that a high temperature will accelerate the decomposition of TNTA. The maximum amounts of NO_2, NO, CO_2, and N_2 increased with the temperature increase. However, for NO_3, the change rule was just the opposite. These results imply that higher temperatures can better promote the production of stable products.

Table 3 demonstrates the relatively higher NF of the reactions at 2500 K and 3500 K. We selected the two temperatures (3500 K, the higher in the series) to illustrate the main trends because of the higher number of reactions.

Table 3. Evolution details of various species.

Species	Appearance Time (ps)			Life Time (fs)			Max Numbers		
	1800 K	2500 K	3500 K	1800 K	2500 K	3500 K	1800 K	2500 K	3500 K
NO_2	0.3	0.3	0.3	2616	2384	1343	53	91	106
NO	4.2	0.3	0.3	1032	1160	1090	17	39	53
NO_3	15.9	3.3	0.6	4629	1771	568	21	10	9
CO_2	24	2.1	0.9	17,561	14,017	4494	138	265	256
N_2	35.1	4.2	1.2	48,558	25,722	11,026	150	282	284

One of the major intermediate species of the maximum net flux of TNTA is C_2O_4 ($2CO_2 \rightarrow C_2O_4$ (R2)), corresponding to reaction 61 after reversible reaction just shown as Table 4. Another major intermediate is C_3O_5 and this molecule appeared at $CO_2 + C_2O_3 \rightarrow C_3O_5$ (R12), corresponding to reaction 15. From the global point of view, we observed two main trends: (a) the important reactions of CO_2 abstraction (R3, 4, 6, 12, 16, 18, 21, 26, 29, 30) that occurred due to the high concentration of CO_2; (b) the breakdown of fragments generating CO_2 (R1, 2, 5, 7, 15, 17, 22, 23, 24, 25, 26, 27) that occurred due to the stability of CO_2. Conversely, the overall analysis of simulations shows that the other main gas product is N_2. The chemical effect of N_2 can be expressed in terms of two types of reactions: R-C-N_2 $\rightarrow$ N_2 + R-C (R1, 9, 10, 20, 28) and R-N-N_2 $\rightarrow$ N_2 + R-N (R8, 13). Thus, in general, increases in CO_2 and N_2 production in the thermal decomposition of TNTA at high temperatures are expected.

Table 4. Elementary reactions and net flux (NF).

2500 K			3500 K		
No.	Reactions	NF	No.	Reactions	NF
R0	$CO_2N_2 \rightarrow N_2 + CO_2$	1053	R0	$CO_2 + N_2 \rightarrow CO_2N_2$	3116
R1	$N_2 + CO_2 \rightarrow CO_2N_2$	1050	R1	$CO_2N_2 \rightarrow CO_2 + N_2$	3103
R2	$C_2O_4 \rightarrow 2\ CO_2$	531	R2	$C_2O_4 \rightarrow 2\ CO_2$	2590
R3	$CO_3N \rightarrow CO_2 + ON$	499	R3	$2\ CO_2 \rightarrow C_2O_4$	2539
R4	$2\ CO_2 \rightarrow C_2O_4$	499	R4	$CO_2 + CO \rightarrow C_2O_3$	604
R5	$CO_2 + ON \rightarrow CO_3N$	498	R5	$C_2O_3 \rightarrow CO_2 + CO$	599
R6	$CO_4N \rightarrow CO_2 + O_2N$	260	R6	$CO_2 + ON \rightarrow CO_3N$	454
R7	$CO_2 + O_2N \rightarrow CO_4N$	254	R7	$CO_3N \rightarrow CO_2 + ON$	448
R8	$ON_3 \rightarrow N_2 + ON$	251	R8	$N_4 \rightarrow 2\ N_2$	400
R9	$N_2 + ON \rightarrow ON_3$	245	R9	$2\ N_2 \rightarrow N_4$	394
R10	$2\ ON \rightarrow O_2N_2$	197	R10	$CON_2 \rightarrow N_2 + CO$	337
R11	$O_2N_2 \rightarrow 2\ ON$	175	R11	$N_2 + CO \rightarrow CON_2$	327
R12	$2\ O_2N \rightarrow O_4N_2$	149	R12	$CO_2 + C_2O_3 \rightarrow C_3O_5$	294
R13	$CO_2 + CO \rightarrow C_2O_3$	143	R13	$ON_3 \rightarrow N_2 + ON$	292
R14	$CON_2 \rightarrow N_2 + CO$	142	R14	$N_2 + ON \rightarrow ON_3$	291
R15	$O_4N_2 \rightarrow 2\ O_2N$	128	R15	$C_3O_5 \rightarrow CO_2 + C_2O_3$	279
R16	$C_2O_3 \rightarrow CO_2 + CO$	122	R16	$C_2O_4 + CO_2 \rightarrow C_3O_6$	197
R17	$N_2 + CO \rightarrow CON_2$	121	R17	$C_3O_6 \rightarrow C_2O_4 + CO_2$	189

Table 4. *Cont.*

2500 K			3500 K		
No.	**Reactions**	**NF**	**No.**	**Reactions**	**NF**
R18	$CON + ON \rightarrow CO_2N_2$	114	R18	$CO_2 + CO_3 \rightarrow C_2O_5$	178
R19	$N_2 + CON \rightarrow CON_3$	111	R19	$N_2 + C_2O_3 \rightarrow C_2O_3N_2$	166
R20	$CON_3 \rightarrow N_2 + CON$	108	R20	$C_2O_3N_2 \rightarrow N_2 + C_2O_3$	164
R21	$C_2O_3N \rightarrow CO_2 + CON$	98	R21	$CO_2 + O_2N \rightarrow CO_4N$	152
R22	$O_3N_2 \rightarrow O_2N + ON$	92	R22	$C_2O_5 \rightarrow CO_2 + CO_3$	142
R23	$CO_2N_2 \rightarrow CON + ON$	85	R23	$CO_4 \rightarrow CO_2 + O_2$	134
R24	$O_2N + ON \rightarrow O_3N_2$	84	R24	$C_2O_4N_2 \rightarrow 2\ CO_2 + N_2$	134
R25	$CO_2 + CON \rightarrow C_2O_3N$	83	R25	$CO_4N \rightarrow CO_2 + O_2N$	131
R26	$O_2N_2 + ON \rightarrow O_3N_3$	79	R26	$C_2O_4 + CO_2 \rightarrow C_2O_4 + CO_2$	131
R27	$C_3O_6N_6 \rightarrow O_2N + C_3O_4N_5$	78	R27	$C_3O_6 \rightarrow 3\ CO_2$	127
R28	$CO_2 + C_2O_3 \rightarrow C_3O_5$	78	R28	$C_2O_4N_2 \rightarrow C_2O_4 + N_2$	124
R29	$C_3O_5 \rightarrow CO_2 + C_2O_3$	77	R29	$CO_2 + O_2 \rightarrow CO_4$	122
R30	$N_4 \rightarrow 2\ N_2$	76	R30	$2\ CO_2 + N_2 \rightarrow C_2O_4N_2$	121

4. Conclusions

We report predictions using quantum mechanics of the most stable crystal structures of TNTA, which is a promising green high-energy-density material. Firstly, the partial RESP charges were used with the COMPASS force field to find the main nonbonded interactions which may affect the space groups. Then, unit cell parameters, Hirshfeld surface analysis, and fingerprint plots of the seven space groups were used to predict the most promising space groups and packings. Finally, the thermal decomposition of TNTA was researched by reactive molecular dynamics using ReaxFF-lg. We found that the $Pna2_1$ space group with the corresponding cell parameters of Z = 4, a = 8.69 Å, b = 9.07 Å, c = 9.65 Å, and $\alpha = \beta = \gamma = 90.0^\circ$ was the most compatible with TNTA. The pyrolysis mechanism implies that increasing the temperature can accelerate the decomposition rate of TNTA. The two main products, CO_2 and N_2, had the same variation trend, and the amount of N_2 was slightly higher than that of CO_2 during the whole reaction time.

Author Contributions: Supervision, D.X.; Writing—original draft, M.-M.Z.; Writing—review & editing, D.X. All authors have read and agreed to the published version of the manuscript.

Funding: This research received no external funding.

Institutional Review Board Statement: Not applicable.

Informed Consent Statement: Not applicable.

Acknowledgments: This work was supported by the Yangtze University Youth Foundation. The authors are grateful to reviewers for very careful reading and helpful suggestions.

Conflicts of Interest: The authors declare no conflict of interest.

References

1. Finger, H. Über abkömmlinge des cyanurs. (Vorläufige Mitteilung). *J. Prakt. Chem.* **1907**, *75*, 103–104. [CrossRef]
2. Immirzi, A.; Pernir, B. Prediction of density in organic crystals. *Acta Crystallogr. A* **1977**, *33*, 216–218. [CrossRef]
3. Korkin, A.A.; Bartlett, R.J. Theoretical prediction of 2,4,6-trinitro-1,3,5-triazine (TNTA). A new, powerful, high-energy density material? *J. Am. Chem. Soc.* **1996**, *118*, 12244–12245. [CrossRef]
4. Yang, K.; Park, Y.H.; Cho, S.G.; Lee, H.W.; Kim, C.K.; Koo, H.J. Theoretical studies on the formation mechanism and explosive performance of nitro-substituted 1,3,5-triazines. *J. Comput. Chem.* **2010**, *31*, 2483–2492. [CrossRef]
5. Desiraju, G.R.; Parshall, G.W. Crystal engineering: The design of organic solids. *Mater. Sci. Monogr.* **1989**, *54*, XIV-312.
6. Desiraju, G.R. Crystal engineering: From molecule to crystal. *J. Am. Chem. Soc.* **2013**, *135*, 9952–9967. [CrossRef]
7. Ma, Y.; Meng, L.; Li, H.; Zhang, C. Enhancing intermolecular interactions and their anisotropy to build low-impact-sensitivity energetic crystals. *CrystEngComm* **2017**, *19*, 3145–3155. [CrossRef]
8. Ma, Y.; Zhang, A.; Xue, X.; Jiang, D.; Zhu, Y.; Zhang, C. Crystal packing of impact-sensitive high-energy explosives. *Cryst. Growth Des.* **2014**, *14*, 6101–6114. [CrossRef]

9. Ma, Y.; Zhang, A.; Zhang, C.; Jiang, D.; Zhu, Y.; Zhang, C. Crystal packing of low-sensitivity and high-energy explosives. *Cryst. Growth Des.* **2014**, *14*, 4703–4713. [CrossRef]
10. Bu, R.; Xiong, Y.; Wei, X.; Li, H.; Zhang, C. Hydrogen bonding in CHON-containing energetic crystals: A review. *Cryst. Growth Des.* **2019**, *19*, 5981–5997. [CrossRef]
11. Liu, G.; Gou, R.; Li, H.; Zhang, C. Polymorphism of energetic materials: A comprehensive study of molecular conformers, crystal packing, and the dominance of their energetics in governing the most stable polymorph. *Cryst. Growth Des.* **2018**, *18*, 4174–4186. [CrossRef]
12. Zhang, C.; Jiao, F.; Li, H. Crystal engineering for creating low sensitivity and highly energetic materials. *Cryst. Growth Des.* **2018**, *18*, 5713–5726. [CrossRef]
13. Graser, J.; Kauwe, S.K.; Sparks, T.D. Machine learning and energy minimization approaches for crystal structure predictions: A review and new horizons. *Chem. Mater.* **2018**, *30*, 3601–3612. [CrossRef]
14. Naserifar, S.; Zybin, S.; Ye, C.C.; Goddard, W.A., III. Prediction of structures and properties of 2,4,6-triamino-1,3,5-triazine-1,3,5-trioxide (MTO) and 2,4,6-trinitro-1,3,5-triazine-1,3,5-trioxide (MTO_3N) green energetic materials from DFT and ReaxFF molecular modeling. *J. Mater. Chem. A* **2016**, *4*, 1264–1276. [CrossRef]
15. Li, H.J.; Liu, J.C.; Yang, L.; Yan, Z.Z.; Lu, Y.W.; Han, J.M.; Li, W. Theoretical predict structure and property of the novel CL-20/2,4-DNI cocrystal by systematic search approach. *Def. Technol.* 2021, in press. [CrossRef]
16. Chen, L.; Wang, H.; Wang, F.; Geng, D.; Wu, J.; Lu, J. Thermal decomposition mechanism of 2,2′,4,4′,6,6′-hexanitrostilbene by ReaxFF reactive molecular dynamics simulations. *J. Phys. Chem. C* **2018**, *122*, 19309–19318. [CrossRef]
17. Song, L.; Zhao, F.Q.; Xu, S.Y.; Ju, X.H. Reactive molecular dynamics simulation of the high-temperature pyrolysis of 2,2′,2′′,4,4′,4′′,6,6′,6′′-nonanitro-1,1′:3′,1′′-terphenyl (NONA). *RSC Adv.* **2020**, *10*, 5507–5515. [CrossRef]
18. Song, L.; Zhao, F.Q.; Xu, S.Y.; Ye, C.C.; Ju, X.H. Structural evolution of aluminum hydride nanoparticles in water using ReaxFF molecular dynamics method. *Mater. Today Commun.* **2021**, *26*, 101804. [CrossRef]
19. Mei, Z.; An, Q.; Zhao, F.Q.; Xu, S.Y.; Ju, X.H. Reactive molecular dynamics simulation of thermal decomposition for nano-aluminized explosives. *Phys. Chem. Chem. Phys.* **2018**, *20*, 29341–29350. [CrossRef]
20. Frisch, M.J. gaussian16. 2020. Available online: http://www.gaussian.com/ (accessed on 11 March 2022).
21. Lu, X.; Clements-Croome, D.; Viljanen, M. Fractal geometry and architecture design: Case study review. *Chaotic Model. Simul. (CMSIM)* **2012**, *2*, 311–322.
22. Lyu, K.; Peng, Y.; Xiao, L.; Lu, J.; Zhuang, L. Water induced phase segregation in hydrocarbon proton exchange membranes. *J. Energy Chem.* **2018**, *27*, 1517–1520. [CrossRef]
23. Spackman, M.A.; Jayatilaka, D. Hirshfeld surface analysis. *CrystEngComm* **2009**, *11*, 19–32. [CrossRef]
24. Turner, M.J.; Grabowsky, S.; Jayatilaka, D.; Spackman, M.A. Accurate and efficient model energies for exploring intermolecular interactions in molecular crystals. *J. Phys. Chem. Lett.* **2014**, *5*, 4249–4255. [CrossRef] [PubMed]
25. Spackman, M.A.; McKinnon, J.J. Fingerprinting intermolecular interactions in molecular crystals. *CrystEngComm* **2002**, *4*, 378–392. [CrossRef]
26. McKinnon, J.J.; Fabbiani, F.P.; Spackman, M.A. Comparison of polymorphic molecular crystal structures through Hirshfeld surface analysis. *Cryst. Growth Des.* **2007**, *7*, 755–769. [CrossRef]
27. McKinnon, J.J.; Spackman, M.A.; Mitchell, A.S. Novel tools for visualizing and exploring intermolecular interactions in molecular crystals. *Acta Crystallogr. Sect. B Struct. Sci.* **2004**, *6*, 627–628.
28. McKinnon, J.J.; Jayatilaka, D.; Spackman, M.A. Towards quantitative analysis of intermolecular interactions with Hirshfeld surfaces. *Chem. Commun.* **2007**, *37*, 3814–3816. [CrossRef]
29. Hamilton, B.W.; Kroonblawd, M.P.; Islam, M.M.; Strachan, A. Sensitivity of the shock initiation threshold of 1,3,5-triamino-2,4,6-trinitrobenzene (TATB) to nuclear quantum effects. *J. Phys. Chem. C* **2019**, *123*, 21969–21981. [CrossRef]
30. Mighell, A.D.; Himes, V.L.; Rodgers, J.R. Space-group frequencies for organic compounds. *Acta Crystallogr. A* **1983**, *39*, 737–740. [CrossRef]
31. Wilson, A.J.C. Space groups rare for organic structures. I. Triclinic, monoclinic and orthorhombic crystal classes. *Acta Crystallogr. A* **1988**, *44*, 715–724. [CrossRef]
32. Baur, W.H.; Kassner, D. The perils of Cc: Comparing the frequencies of falsely assigned space groups with their general population. *Acta Crystallogr B* **1992**, *48*, 356–369. [CrossRef]
33. Belsky, V.K.; Zorkii, P.M. Distribution of organic homomolecular crystals by chiral types and structural classes. *Acta Crystallogr. A* **1977**, *33*, 1004–1006. [CrossRef]
34. Wang, Y.; Song, S.; Huang, C.; Qi, X.; Wang, K.; Liu, Y.; Zhang, Q. Hunting for advanced high-energy-density materials with well-balanced energy and safety through an energetic host-guest inclusion strategy. *J. Mater. Chem. A* **2019**, *7*, 19248–19257. [CrossRef]
35. Ding, R.; Xu, J.; Tao, Y.; Sun, J.; Lei, M. Experimental and theoretical study on the stability of CL-20-based host-guest energetic materials. *J. Phys. Chem. A* **2020**, *124*, 6389–6398. [CrossRef]
36. Spackman, M.A.; Byrom, P.G. A novel definition of a molecule in a crystal. *Chem. Phys. Lett.* **1997**, *267*, 215–220. [CrossRef]